
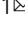



Large flux-mediated coupling in hybrid electromechanical system with a transmon qubit

Tanmoy Bera^{1,2}, Sourav Majumder^{1,2}, Sudhir Kumar Sahu¹ & Vibhor Singh¹  

Control over the quantum states of a massive oscillator is important for several technological applications and to test the fundamental limits of quantum mechanics. Addition of an internal degree of freedom to the oscillator could be a valuable resource for such control. Recently, hybrid electromechanical systems using superconducting qubits, based on electric-charge mediated coupling, have been quite successful. Here, we show a hybrid device, consisting of a superconducting transmon qubit and a mechanical resonator coupled using the magnetic-flux. The coupling stems from the quantum-interference of the superconducting phase across the tunnel junctions. We demonstrate a vacuum electromechanical coupling rate up to 4 kHz by making the transmon qubit resonant with the readout cavity. Consequently, thermal-motion of the mechanical resonator is detected by driving the hybridized-mode with mean-occupancy well below one photon. By tuning qubit away from the cavity, electromechanical coupling can be enhanced to 40 kHz. In this limit, a small coherent drive on the mechanical resonator results in the splitting of qubit spectrum, and we observe interference signature arising from the Landau-Zener-Stückelberg effect. With improvements in qubit coherence, this system offers a platform to realize rich interactions and could potentially provide full control over the quantum motional states.

¹Department of Physics, Indian Institute of Science, Bangalore 560012, India. ²These authors contributed equally: Tanmoy Bera, Sourav Majumder. email: v.singh@iisc.ac.in

Cavity optomechanical systems, where a mechanical mode parametrically modulates the resonant frequency of an electromagnetic (EM) mode, have been very successful in controlling the motional states of massive oscillators¹. Starting from the earlier demonstration of the motional quantum ground state by the sideband cooling technique^{2,3}, these experiments have reached several milestones related to the displacement-detection⁴ and the preparation of the non-classical states of mechanical motion^{5,6}. Beyond the traditional two-mode systems, consisting of one EM and one mechanical mode, cavity optomechanical systems with an auxiliary mode provides a wide range of interactions. Such systems have been used to realize non-reciprocal devices^{7–9}, and to demonstrate quantum entanglement between two mechanical resonators^{10,11}.

Among the two-mode cavity optomechanical devices, preparation of the quantum states of motion appears to be technologically challenging. One successful strategy in the microwave domain, to circumvent this, is to introduce an auxiliary nonlinear mode such as a qubit. The qubit can be used as a single-photon source¹², photon-counter¹³, or directly coupled to a mechanical mode using its charge dispersion^{14–17} or the piezo-electric effect^{18–20}. In such devices, the qubit mode “acts” like an additional degree of freedom which couples to mechanical mode via an intermediate mode or directly using the “charge” dispersion.

While systems utilizing the charge-based coupling have been studied extensively, the experimental progress of the hybrid systems based on magnetic-flux has been very limited. Here we design and study the performance of a hybrid electromechanical device based on a fundamentally different coupling scheme based on the magnetic flux. We engineer the device parameters such that in addition to the flux-based electromechanical coupling, one mode maintains sufficient anharmonicity to be qualified as a qubit. This approach results in an electromechanical system with an internal spin-half degree of freedom. By recording the thermomechanical motion of the resonator, we demonstrate a magnetic field tunable electromechanical coupling rate up to 4 kHz when qubit is tuned in resonance with the cavity. On one hand, the strong and tunable nonlinearity of the qubit mode improves the displacement sensitivity. On the other hand, the large electromechanical coupling modifies the qubit spectrum in the dispersive limit. As a consequence, we observe the Landau–Zener–Stückelberg (LZS) interference in the qubit spectrum when the qubit is detuned in the dispersive limit. Similar to vacuum-electromechanical coupling rate’s scaling with total charge in charge-dispersion-based schemes^{14–16}, the coupling rate here scales linearly with the magnetic field. Therefore, such an approach has the potential to reach the elusive single-photon strong coupling regime with suitable choice of materials²¹.

Results and discussion

Concept. The hybrid device consists of a transmon qubit coupled to a mechanical resonator and a readout cavity, as shown in Fig. 1a. The transmon qubit couples to the cavity via a dipole coupling, commonly referred to as transverse coupling, as it connects the ground and the first excited state of the qubit²². The mechanical resonator couples to the qubit via a flux-mediated coupling. Such coupling is achieved by embedding a mechanical resonator into one of the arms of a SQUID (Superconducting Quantum Interference Device) loop, which provides the necessary Josephson inductance to form a transmon qubit. Due to the quantum interference of the superconducting phase, the Josephson inductance of the SQUID depends on the magnetic flux threading the loop as schematically shown in Fig. 1b. In the presence of a magnetic field, applied normal to the plane of the SQUID, it acts like a displacement-dependent nonlinear inductor.

By shunting the SQUID “inductor” to a suitable capacitance, a transmon qubit mode can be designed. As the motion of the mechanical resonator directly affects the qubit transition frequency, this coupling is referred to as longitudinal coupling. A flux-coupled hybrid system formed this way can be thought of a dual to the “charge” coupling approach realized with the Cooper-pair box qubit¹⁶.

Theoretically, the flux-mediated electromechanical coupling has been considered in the context of flux-qubits²³, cavity-electromechanical devices²⁴, and more recently with the transmon qubit^{21,25}. On the experimental side, the scheme has been used for large bandwidth displacement detection²⁶, and to demonstrate the cavity-electromechanical system by embedding Josephson elements in the microwave circuitry^{27,28}.

In comparison to existing flux-coupling approaches^{27,28}, our design methodology circumvents several issues by using a tunable transmon mode. First, the requirement of large Josephson inductance for transmon design helps in suppressing hysteretic effects with magnetic flux arising from geometrical and kinetic inductance. Second, our approach here is to implement a longitudinal coupling between transmon qubit and a mechanical resonator through the modulation of Josephson inductance. This enables the interaction of the mechanical mode with the qubit in two distinct ways. First, due to strong coupling between the qubit and cavity in the resonant limit, the mechanical motion directly couples to the hybridized states. Second, in the dispersive limit when the qubit is detuned far away from the cavity, a sufficiently large coupling between the qubit and the mechanical mode can be maintained. It thus provides a mean to use the qubit as an internal degree of freedom to the mechanical mode and further paves ways for measurement-based cooling and control protocols^{25,29,30}.

Device design. We use a three-dimensional (3D) cavity to implement the transmon design as shown schematically in Fig. 1c. Unlike the conventional 3D-transmon qubit, which couples differentially to the cavity mode, we design a single-ended qubit mode by grounding one end of the SQUID loop to the cavity wall using a small wirebond³¹. The other end of the SQUID loop extends toward the center of the cavity and provides the necessary qubit capacitance and coupling with the fundamental cavity mode. The rectangular cavity ($35 \times 4 \times 35 \text{ mm}^3$) is machined using copper with the fundamental resonant mode TE_{101} at $\omega_c \approx 2\pi \times 6 \text{ GHz}$. A false-color scanning electron microscope (SEM) image of the SQUID loop is shown in Fig. 1d. The nanobeam-shaped mechanical resonator, formed by a 100-nm highly stressed SiN film coated with 50 nm of aluminum, and suspended part of the Josephson junctions can be clearly seen. Important device parameters are listed in the Supplementary Note 1. The offset in the SQUID position (away from the center of the cavity) in transmon design allows us to bring a RF drive line for the electrostatic actuation of the mechanical resonator. Results from design simulations are included in the Supplementary Note 3.

The transmon qubit frequency ω_q is given by $\hbar\omega_q \approx \sqrt{8E_C E_J^0 |\cos(\pi\Phi/\Phi_0)| - E_C}$, where E_J^0 is the maximum Josephson energy, E_C is the charging energy, Φ is the total flux threading the SQUID loop, and $\Phi_0 = h/2e$ is the magnetic flux quanta. The tunability of qubit frequency with flux allows access to its dispersive or resonant interaction with the cavity. The interaction between the qubit and the cavity mode can be expressed as $\hbar J(\hat{a}\hat{\sigma}^+ + \hat{a}^\dagger\hat{\sigma}^-)$, where $\hat{a}(\hat{\sigma}^-)$ is the ladder operator for the cavity (qubit) mode and J is the dipole coupling rate. The electromechanical coupling arises from the modulation of qubit

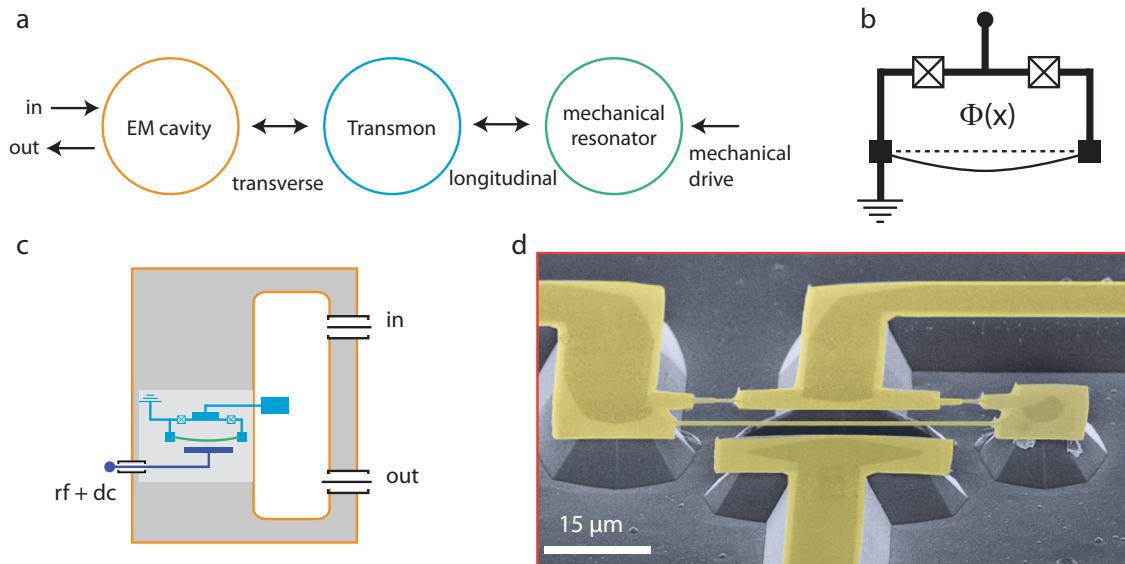


Fig. 1 Device concept and design. **a** A schematic showing various components of the hybrid electromechanical system. The transmon qubit couples to an electromagnetic cavity via the transverse coupling. A low-frequency mechanical resonator couples to the transmon qubit via the longitudinal coupling. **b** A schematic of the SQUID loop with a suspended arm. Due to the magnetic flux $\Phi(x)$ dependence of Josephson inductance, it forms a displacement-dependent inductor. **c** A cross-sectional view of a 3D-cavity based transmon device. The gray (white) portion represents the copper (machined chamber). Input-output ports for microwave and a third port added for mechanical actuation is shown. The SQUID loop is placed inside a small recess of the cavity schematically shown by the lighter gray area. **d** A false-color scanning electron microscope image of the SQUID loop, showing the suspended portion of the Josephson junctions and the nanobeam. The mechanical resonator has a length and width of $45\ \mu\text{m}$ and $300\ \text{nm}$, respectively. It consists of a 50-nm coating of aluminum over a 100-nm -thick highly stressed SiN film. The T-shaped electrode in the lower-half of the image is used to actuate the mechanical resonator.

frequency caused by mechanical displacement. As the qubit frequency can be tuned over a large range, it is convenient to define the vacuum electromechanical coupling rate between the qubit-cavity hybridized states (ω_{\pm}) and the mechanical resonator as,

$$g_{\pm}(\Phi) = \frac{\partial \omega_{\pm}(\Phi)}{\partial x} x_{zp} = \Phi G_{\Phi}^{\pm} \frac{x_{zp}}{w}, \quad (1)$$

where $G_{\Phi}^{\pm} = \partial \omega_{\pm}(\Phi)/\partial \Phi$ is the flux-responsivity, x_{zp} is the quantum zero-point fluctuations of the mechanical resonator, and w is the effective width of the SQUID loop. Equation (1) defines the coupling rate over the entire range of qubit frequencies. The hybridized modes $\omega_{\pm} = \bar{\Delta} \pm \sqrt{(\Delta/2)^2 + J^2}$ with $\Delta = \omega_q - \omega_c$, $\bar{\Delta} = (\omega_q + \omega_c)/2$ approach the uncoupled qubit and cavity frequencies in the dispersive limit. Restricting the coupled qubit-cavity system to single excitation subspace, in the resonant limit $|\Delta| \ll J$, the hybridized modes essentially act like independent cavity optomechanical systems. However, it is worth pointing out here that the interaction between the hybridized modes and the mechanical motion can be used to enhance the quantum nonlinearity by designing J comparable to the mechanical frequency^{32,33}.

Qubit spectroscopy and flux-responsivity. We use spectroscopic measurements to characterize the qubit. Figure 2a shows the transmission ($|S_{21}(\omega)|$) through the cavity as applied magnetic flux is varied. When the qubit becomes resonant with the cavity, the vacuum Rabi splitting is observed which signifies the strong coupling between the qubit and cavity mode. We determine a dipole coupling rate $J = 2\pi \times 85\ \text{MHz}$, the bare cavity frequency $\omega_c = 2\pi \times 5.993\ \text{GHz}$, maximum qubit frequency $\omega_q^0 = 2\pi \times 7.982\ \text{GHz}$, and an anharmonicity of $-132\ \text{MHz}$ (see the Supplementary Note 4 for details). Due to the flux-periodicity

of qubit frequency, the vacuum Rabi splitting pattern repeats with every new flux-quantum added. The extension panel of Fig. 2a shows the transmission measurement at a higher magnetic field. Apart from a small reduction ($\sim 15\ \text{MHz}$) in the maximum qubit frequency and an increase in the dressed-cavity mode linewidth, we do not observe any significant change in the device parameters up to a field of $\sim 3.7\ \text{mT}$ ($310\ \Phi_0$).

To understand the flux-transduction of hybridized modes, we compute the flux-responsivity G_{Φ}^{\pm} using the measured qubit and cavity parameters and assuming identical junctions. Figure 2b shows the plot of G_{Φ}^{\pm} with respect to the hybridized-mode frequencies. The flux-responsivity of the hybridized modes increases as their relative detuning ($|\omega_{\pm} - \omega_c|$) increases. However, reduced transmission at frequencies far away from ω_c hinders their use for the mechanical transduction. We choose an optimum operating point of $6.025\ \text{GHz}$, corresponding to $G_{\Phi}^{\pm}/2\pi \sim 1.8\ \text{GHz}/\Phi_0$, for the mechanical resonator characterization. This flux-responsivity is significantly larger than the values reported with the SQUID cavity²⁷. In addition, the flux-responsivity of qubit $G_{\Phi}^q = \partial \omega_q/\partial \Phi$ can be much larger near the half-integer flux quantum as shown in Fig. 2c. In the dispersive limit, while the effective coupling between the dressed cavity and mechanical resonator degrades by a factor of $(J/\Delta)^2$, a large coupling between the qubit and the mechanical resonator can be maintained.

Detection of mechanical mode and vacuum electromechanical rate. We first focus on the driven response of the mechanical resonator. For electrostatic actuation, a weak ac signal and a dc voltage V_{dc} are applied at the mechanical drive port. We fine-tune the magnetic flux near $190\ \Phi_0$ to operate the hybridized mode $\omega_+/2\pi$ at $6.025\ \text{GHz}$. We inject a microwave tone at ω_+ creating a mean photon occupation of ≈ 1 , calibrated independently using ac-Stark shift. Details are provided in the Supplementary Note 5.

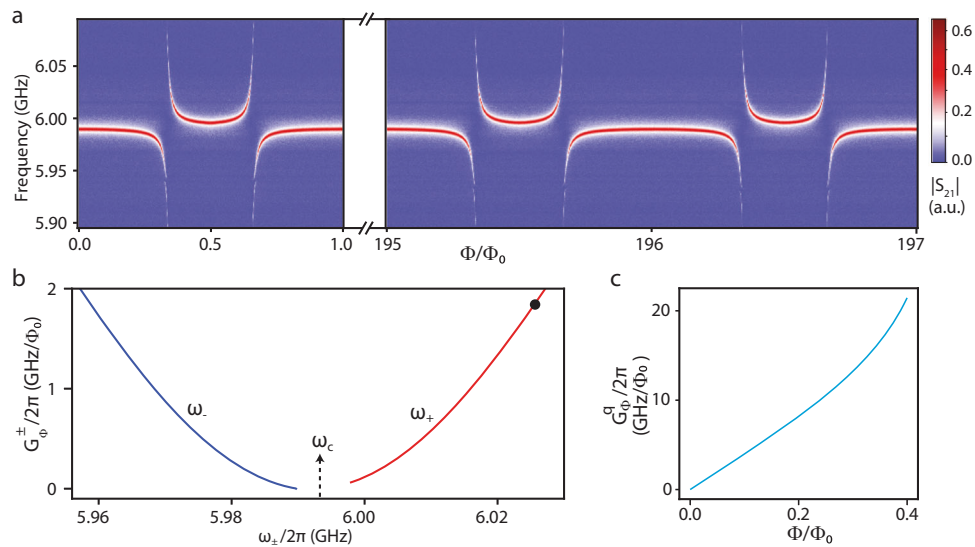


Fig. 2 Measurement of the flux responsivity. **a** Color scale plot of transmission $|S_{21}|$ through the cavity as the magnetic flux through the SQUID loop is varied. The strong qubit-cavity coupling (J) manifests as the avoided crossing, yielding $J \sim 2\pi \times 85$ MHz. The extension panel shows the trend of avoided crossing at larger values of the magnetic flux. **b** The flux-responsivity $G_{\Phi}^{\pm} = \partial\omega_{\pm}/\partial\Phi$, computed using the measured device parameters, assuming identical junctions, plotted as a function of hybridized frequencies. The black dot denotes the operating point of 6.025 GHz, corresponding to $G_{\Phi}^{+}/2\pi \sim 1.8$ GHz/ Φ_0 for the subsequent measurements. The arrow indicates the bare cavity frequency $\omega_c/2\pi \sim 5.993$ GHz. **c** The flux-responsivity of uncoupled qubit $G_{\Phi}^q = \partial\omega_q/\partial\Phi$ with the magnetic flux.

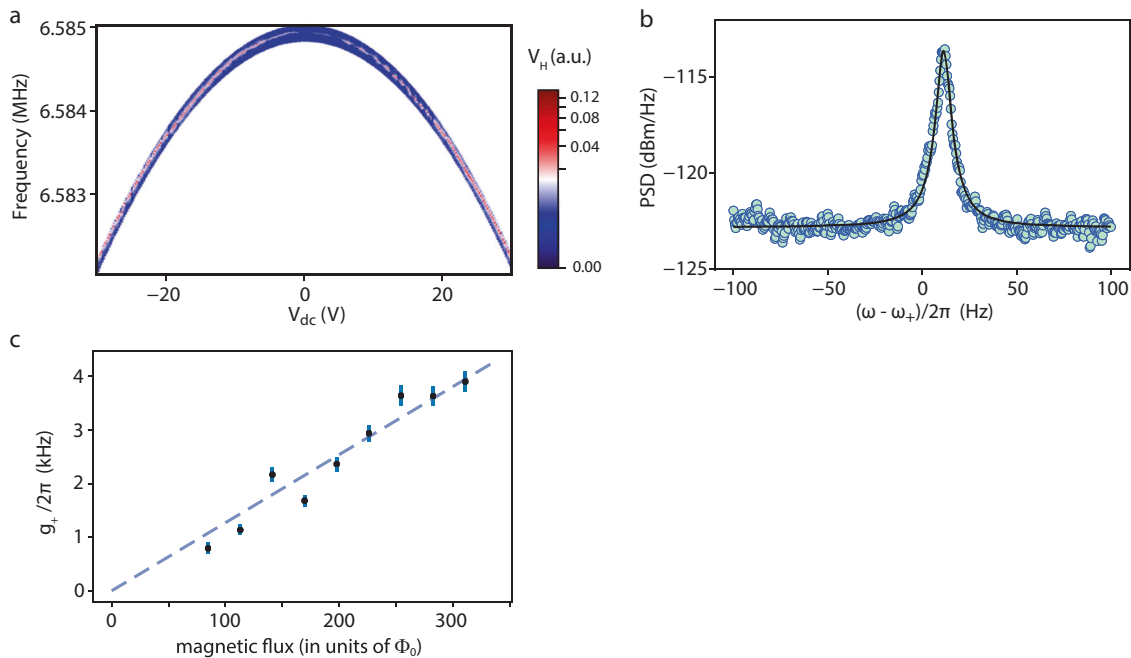


Fig. 3 Characterization of mechanical mode and electromechanical coupling rate. **a** Color plot of the mixed-down signal V_H as mechanical actuation frequency and dc voltage is varied. The mechanical resonance appears as a sharp change in the color. Blue(red) color represents low(high) values of the signal. To reduce the total measurement time, the mechanical actuation frequency range is automatically adjusted to follow the mechanical mode. **b** Average power spectral density (PSD) along with a fitted curve yielding a mechanical linewidth $\gamma_m \sim 2\pi \times 6$ Hz corresponding to a quality factor of $\sim 1.1 \times 10^6$. **c** Plot of the vacuum electromechanical coupling rate between hybridized mode and the mechanical resonator as the magnetic flux through the SQUID loop is increased, while $\omega_{+} = 2\pi \times 6.025$ GHz is kept fixed. The maximum flux applied corresponds to a field of 3.7 mT. The blue-dotted line shows the expected coupling rate calculated from the device parameters. The error bars represent the uncertainty resulting from the numerical fit of the PSD.

The signal that emerges from the cavity is then mixed-down and recorded by a network analyzer. Figure 3a shows the amplitude of the signal in a color plot as the mechanical drive frequency and V_{dc} are varied. The change in color over the background signifies the mechanical resonance. We measure the in-plane vibrational

mode at $\omega_m \sim 2\pi \times 6.585$ MHz with a characteristic capacitive frequency softening with V_{dc} .

Next, we focus on the thermal motion of the mechanical resonator. We operate the hybridized mode at $\omega_{+} = 2\pi \times 6.025$ GHz and drive the system with a microwave tone tuned to lower

sideband ($\omega_+ - \omega_m$), creating a mean photon occupation of ~ 0.1 . The power spectral density (PSD) of the output signal is then recorded with a spectrum analyzer. The average PSD, along with the fitted Lorentzian, is shown in Fig. 3b. We measure a mechanical linewidth of $\gamma_m = 2\pi \times 6$ Hz, corresponding to a quality factor of $\sim 1.1 \times 10^6$.

For a drive at the lower sideband, the ratio of integrated power at the up-converted frequency (P_m) near ω_+ to the power of transmitted carrier signal (P_d) at $\omega_+ - \omega_m$ can be conveniently expressed as $P_m/P_d = (2g_+/\kappa)^2 n_m^{\text{th}}$, where n_m^{th} is the mean thermal occupation of the mechanical mode, and κ is the hybridized-mode linewidth. To estimate the thermal occupation of the mechanical mode, we first measure $(\kappa/2)\sqrt{(P_m/P_d)}$ for different values of applied flux. We fit the expected linear dependence of this quantity on magnetic flux to obtain the slope $\sqrt{n_m^{\text{th}}}(g_+/\Phi)$. By using the estimated value of g_+/Φ from the device parameters (Eq. (1)), we then obtain the thermal phonon occupancy of 169. This corresponds to a mode temperature of 53 ± 4 mK, which is consistent with the independent estimate obtained by varying the fridge temperature (additional details are given in the Supplementary Note 6). Using $n_m^{\text{th}} = 169$, we then calculate the g_+ as shown in Fig. 3c.

We emphasize that the vacuum electromechanical coupling rate of $g_+ \sim 2\pi \times 4$ kHz is limited by choice of ω_+ , and the magnetic field range available in our measurement setup. By operating at $\omega_c \pm J$, one can achieve the $G_{\Phi}^+/G_{\Phi}^q = 1/2$, resulting in $g_+ \sim 2\pi \times 15$ kHz. In addition, thin films of Al can withstand a larger magnetic field than the maximum field used here (3.7 mT). As the in-plane critical magnetic field is much larger than the perpendicular critical magnetic field for thin Al films, a configuration with field applied in-plane to the SQUID loop would result in significantly higher coupling rates for the out-of-plane mechanical mode.

LZS interference in the dispersive limit. Next, we investigate the system by tuning the qubit away from ω_c . In the dispersive limit $|\Delta| \gg J$, the mechanics essentially decouples from the cavity mode. While the qubit-cavity interaction is given by $(J^2/\Delta)\hat{a}^\dagger\hat{a}\hat{\sigma}_z$, the longitudinal interaction between the uncoupled qubit and the mechanical resonator is given by $g_{\text{qm}}\hat{\sigma}_z(\hat{b} + \hat{b}^\dagger)$, where $g_{\text{qm}} = (\partial\omega_q/\partial x)x_{\text{zp}}$ is the qubit-electromechanical coupling rate and $\hat{b}(\hat{b}^\dagger)$ is the lowering (raising) operator for the mechanical mode. With a superconducting qubit device, time-dependent longitudinal coupling scheme has been used to perform high-fidelity qubit measurements³⁴. In the present device, a static g_{qm} would instead result in a small qubit-state-dependent displacement ($\sim g_{\text{qm}}x_{\text{zp}}/\omega_m$)²⁹. Here, we focus on the qubit dynamics while driving the mechanical resonator. The qubit is detuned to 4.9 GHz to enhance g_{qm} to 40 kHz, and its spectrum is probed using the two-tone spectroscopy technique. The mechanical resonator is coherently actuated at its resonant frequency. It is equivalent to the flux-modulation of the qubit frequency at ω_m , and a frequency deviation set by g_{qm} and the mechanical amplitude.

Figure 4a shows the qubit spectrum as the strength of mechanical drive is varied. We observe a splitting in the qubit spectrum with a weak modulation in-between. The separation between the primary splitting varies linearly with the mechanical amplitude. The primary splitting can be understood by considering the passage of the system across the region of avoided crossing with separation set by the strength of the spectroscopic tone (the Rabi-flop rate Ω_R)³⁵. As the system moves across the avoided crossing at a rate set by ω_m , the transition during multiple passages mix the two states, eventually resulting in

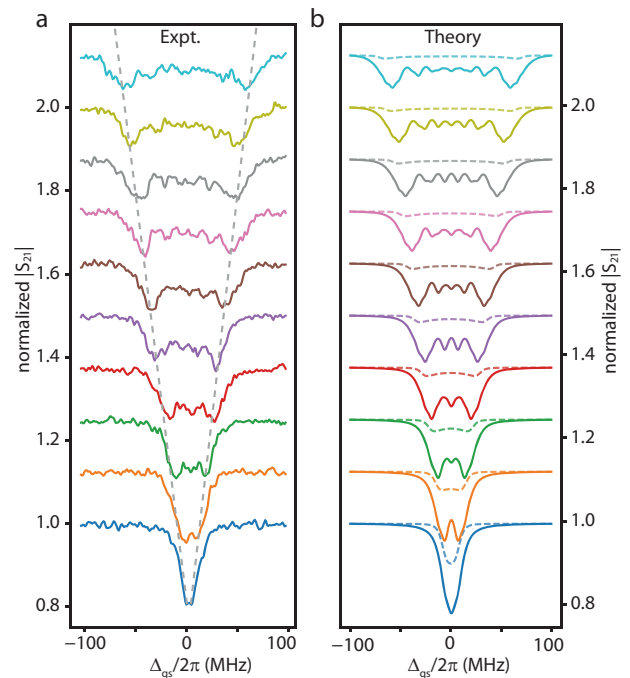


Fig. 4 Qubit spectroscopy and Landau-Zener-Stückelberg interference.

a Measurement of the qubit spectrum with the detuning of spectroscopy tone $\Delta_{\text{qs}} = \omega_s - \omega_q$, where ω_s is the spectroscopy frequency. The mechanical drive signal is varied from 1 to 10 mV in steps of 1 mV (bottom to top). The Rabi flop rate $\Omega_R/2\pi$ is about 3 MHz. Apart from the primary splitting, weak fringes arising from the Landau-Zener-Stückelberg interference are visible. Dotted lines are added as guide to the eye. **b** The solid lines show the results from the Master equation. The dotted lines show the results from semi-classical calculation. Clearly, the calculations performed using the Master equation match the experimental results better. The qubit frequency deviation is changed from 7 MHz to 70 MHz in steps of 7 MHz (bottom to top). A qubit relaxation rate of 2 MHz, and a pure dephasing rate of 4 MHz is used to calculate the qubit spectrum. In both panels, the probe transmission corresponding to the lowest mechanical drive is normalized to one, and an offset of 0.125 has been added successively.

almost equal population of the two energy levels. Hence, it results in the splitting of the qubit spectrum. This splitting of qubit spectrum can be captured in semi-classical calculation as shown by the dotted lines in Fig. 4b. Calculation details are included in the Supplementary Note 7.

At large mechanical drive power, the system crosses avoided-crossing region with higher speed. In this regime, one would expect to see the interference fringes, arising from multiple Landau-Zener transitions, at a separation close to ω_m ³⁵. In our experiment, as the qubit linewidth is comparable to the modulation frequency ω_m , the fringes are not well resolved. Their signatures are visible as weak modulation between the primary splitting. We have performed numerical calculations based on the Lindblad master equation. The solid line in Fig. 4b shows the result from such calculations. Apart from capturing the linear amplitude dependence of the primary splitting, the calculated results show the weak modulation in the experimental data, whereas the semi-classical calculation only shows the primary splitting.

Conclusion. In summary, we have developed a hybrid electro-mechanical device by integrating a modified 3D-transmon qubit

and extremely low-loss mechanical resonator of SiN/Al. The detection of thermo-mechanical motion by driving the system with less than one photon highlights the large underlying coupling rate. Accessibility to different regimes of interaction is further demonstrated by the observation of the LZS interference. Looking ahead, by accessing in-plane vibration mode through changes in the design geometry and in combination with higher magnetic field, the flux coupling rate can be increased. With further improvements in the coupling strength, the device in consideration can reach resolved sideband regime and strong coupling regime. This could enable experiments in the regime of the single-photon cooperativity exceeding one, and conditional cooling of the mechanical resonator to the quantum ground state.

Methods

Device fabrication and measurement setup. For device fabrication, we use an intrinsic Si (100) substrate coated with a 100-nm-thick high-stress SiN layer grown using the low-pressure chemical vapor deposition method. Using standard lithography and shadow evaporation techniques, the transmon design is patterned in a single lithography step. To release the mechanical resonator, a combination of dry and wet etching processes is used. First, the exposed SiN is vertically etched by the reactive ion etching using SF₆ and CHF₃ plasma. The aluminum film naturally acts as a mask layer and thus protects the SiN underneath it. In the second step of etching, a modified-TMAH-based etchant is used to remove the exposed silicon, while providing excellent selectivity against Al and SiN. Additional details are given in the Supplementary Note 2. After the wet etch process, the samples are blow-dried gently with N₂, requiring no critical point drying. The (111)-facets of Si resulted from the wet etch process can also be seen in Fig. 1d. The sample placed inside a copper cavity, along with a small solenoid, is kept inside a cryoperm-shield to protect it from the ambient magnetic field fluctuations.

Data availability

All raw data and processed data as well as supporting code for processing and figure generation are available in Zenodo with the DOI: <https://doi.org/10.5281/zenodo.4314415>.

Received: 21 October 2020; Accepted: 16 December 2020;

Published online: 19 January 2021

References

- Aspelmeyer, M., Kippenberg, T. J. & Marquardt, F. Cavity optomechanics. *Rev. Mod. Phys.* **86**, 1391–1452 (2014).
- Teufel, J. D. et al. Sideband cooling of micromechanical motion to the quantum ground state. *Nature* **475**, 359–363 (2011).
- Chan, J. et al. Laser cooling of a nanomechanical oscillator into its quantum ground state. *Nature* **478**, 89–92 (2011).
- Anetsberger, G. et al. Measuring nanomechanical motion with an imprecision below the standard quantum limit. *Phys. Rev. A* **2**, 061804 (2010).
- Pirkkalainen, J.-M., Damskägg, E., Brandt, M., Massel, F. & Sillanpää, M. A. Squeezing of quantum noise of motion in a micromechanical resonator. *Phys. Rev. Lett.* **115**, 243601 (2015).
- Wollman, E. E. et al. Quantum squeezing of motion in a mechanical resonator. *Science* **349**, 952–955 (2015).
- Peterson, G. A. et al. Demonstration of efficient nonreciprocity in a microwave optomechanical circuit. *Phys. Rev. X* **7**, 031001 (2017).
- Bernier, N. R. et al. Nonreciprocal reconfigurable microwave optomechanical circuit. *Nat. Commun.* **8**, 604 (2017).
- Barzanjeh, S. et al. Mechanical on-chip microwave circulator. *Nat. Commun.* **8**, 1–7 (2017).
- Riedinger, R. et al. Remote quantum entanglement between two micromechanical oscillators. *Nature* **556**, 473–477 (2018).
- Ockeloen-Korppi, C. F. et al. Stabilized entanglement of massive mechanical oscillators. *Nature* **556**, 478–482 (2018).
- Reed, A. P. et al. Faithful conversion of propagating quantum information to mechanical motion. *Nat. Phys.* **13**, 1163–1167 (2017).
- Lecocq, F., Teufel, J. D., Aumentado, J. & Simmonds, R. W. Resolving the vacuum fluctuations of an optomechanical system using an artificial atom. *Nat. Phys.* **11**, 635–639 (2015).
- Pirkkalainen, J.-M. et al. Hybrid circuit cavity quantum electrodynamics with a micromechanical resonator. *Nature* **494**, 211–215 (2013).

- Pirkkalainen, J.-M. et al. Cavity optomechanics mediated by a quantum two-level system. *Nat. Commun.* **6**, 6981 (2015).
- Viennot, J. J., Ma, X. & Lehnert, K. W. Phonon-number-sensitive electromechanics. *Phys. Rev. Lett.* **121**, 183601 (2018).
- Sletten, L. R., Moores, B. A., Viennot, J. J. & Lehnert, K. W. Resolving phonon Fock states in a multimode cavity with a double-slit qubit. *Phys. Rev. X* **9**, 021056 (2019).
- O’Connell, A. D. et al. Quantum ground state and single-phonon control of a mechanical resonator. *Nature* **464**, 697–703 (2010).
- Chu, Y. et al. Creation and control of multi-phonon Fock states in a bulk acoustic-wave resonator. *Nature* **563**, 666 (2018).
- Arrangoiz-Arriola, P. et al. Resolving the energy levels of a nanomechanical oscillator. *Nature* **571**, 537–540 (2019).
- Kounalakis, M., Blanter, Y. M. & Steele, G. A. Flux-mediated optomechanics with a transmon qubit in the single-photon ultrastrong-coupling regime. *Phys. Rev. Res.* **2**, 023335 (2020).
- Koch, J. et al. Charge-insensitive qubit design derived from the Cooper pair box. *Phys. Rev. A* **76**, 042319 (2007).
- Xue, F. et al. Controllable coupling between flux qubit and nanomechanical resonator by magnetic field. *New J. Phys.* **9**, 35–35 (2007).
- Nation, P. D., Suh, J. & Blencowe, M. P. Ultrastrong optomechanics incorporating the dynamical Casimir effect. *Phys. Rev. A* **93**, 022510 (2016).
- Khosla, K. E., Vanner, M. R., Ares, N. & Laird, E. A. Displacement electromechanics: how to detect quantum interference in a nanomechanical resonator. *Phys. Rev. X* **8**, 021052 (2018).
- Etaki, S. et al. Motion detection of a micromechanical resonator embedded in a d.c. SQUID. *Nat. Phys.* **4**, 785–788 (2008).
- Rodrigues, I. C., Bothner, D. & Steele, G. A. Coupling microwave photons to a mechanical resonator using quantum interference. *Nat. Commun.* **10**, 5359 (2019).
- Schmidt, P. et al. Sideband-resolved resonator electromechanics on the single-photon level based on a nonlinear Josephson inductance. *Commun. Phys.* **3**, 233 (2020).
- Didier, N., Bourassa, J. & Blais, A. Fast quantum nondemolition readout by parametric modulation of longitudinal qubit-oscillator interaction. *Phys. Rev. Lett.* **115**, 203601 (2015).
- Leibfried, D., Blatt, R., Monroe, C. & Wineland, D. Quantum dynamics of single trapped ions. *Rev. Mod. Phys.* **75**, 281–324 (2003).
- Barends, R. et al. Coherent Josephson qubit suitable for scalable quantum integrated circuits. *Phys. Rev. Lett.* **111**, 080502 (2013).
- Ludwig, M., Safavi-Naeini, A. H., Painter, O. & Marquardt, F. Enhanced quantum nonlinearities in a two-mode optomechanical system. *Phys. Rev. Lett.* **109**, 063601 (2012).
- Bishop, L. S. et al. Nonlinear response of the vacuum Rabi resonance. *Nat. Phys.* **5**, 105–109 (2009).
- Touzard, S. et al. Gated conditional displacement readout of superconducting qubits. *Phys. Rev. Lett.* **122**, 080502 (2019).
- Shevchenko, S. N., Ashhab, S. & Nori, F. Landau-Zener-Stückelberg interferometry. *Phys. Rep.* **492**, 1–30 (2010).

Acknowledgements

V.S. acknowledges the support received from Infosys Science Foundation, and under the “Early Career Research Award” by SERB, Department of Science and Technology (DST), Govt. of India. T.B. and S.M. thank Tata Trust for providing the travel support. The authors acknowledge device fabrication facilities at CeNSE, IISc, Bangalore, and central facilities at the Department of Physics funded by DST. Authors thank R. Vijayraghavan, Manas Kulkarni, Diptiman Sen, and G. S. Agarwal for valuable discussions.

Author contributions

T.B. and S.M. contributed equally to this work. V.S. conceived the experiments. T.B. and S.M. fabricated the devices. T.B., S.M., and S.K.S. performed the measurements. T.B., S.M., and V.S. performed the data analysis. All the authors contributed to writing of the manuscript and discussing the results.

Competing interests

The authors declare no competing interests.

Additional information

Supplementary information is available for this paper at <https://doi.org/10.1038/s42005-020-00514-y>.

Correspondence and requests for materials should be addressed to V.S.

Reprints and permission information is available at <http://www.nature.com/reprints>

Publisher’s note Springer Nature remains neutral with regard to jurisdictional claims in published maps and institutional affiliations.



Open Access This article is licensed under a Creative Commons Attribution 4.0 International License, which permits use, sharing, adaptation, distribution and reproduction in any medium or format, as long as you give appropriate credit to the original author(s) and the source, provide a link to the Creative Commons license, and indicate if changes were made. The images or other third party material in this article are included in the article's Creative Commons license, unless indicated otherwise in a credit line to the material. If material is not included in the article's Creative Commons license and your intended use is not permitted by statutory regulation or exceeds the permitted use, you will need to obtain permission directly from the copyright holder. To view a copy of this license, visit <http://creativecommons.org/licenses/by/4.0/>.

© The Author(s) 2021